

Cite this: *Nanoscale*, 2011, **3**, 1823

www.rsc.org/nanoscale

PAPER

Mechanical properties of ceria nanorods and nanochains; the effect of dislocations, grain-boundaries and oriented attachment†

Thi X. T. Sayle,^a Beverley J. Inkson,^f Ajay Karakoti,^b Amit Kumar,^b Marco Molinari,^e Günter Möbus,^f Stephen C. Parker,^e Sudipta Seal^{bcd} and Dean C. Sayle^{*a}

Received 14th December 2010, Accepted 9th February 2011

DOI: 10.1039/c0nr00980f

We predict that the presence of extended defects can reduce the mechanical strength of a ceria nanorod by 70%. Conversely, the pristine material can deform near its theoretical strength limit. Specifically, atomistic models of ceria nanorods have been generated with full microstructure, including: growth direction, morphology, surface roughening (steps, edges, corners), point defects, dislocations and grain-boundaries. The models were then used to calculate the mechanical strength as a function of microstructure. Our simulations reveal that the compressive yield strengths of ceria nanorods, *ca.* 10 nm in diameter and without extended defects, are 46 and 36 GPa for rods oriented along [211] and [110] respectively, which represents almost 10% of the bulk elastic modulus and are associated with yield strains of about 0.09. Tensile yield strengths were calculated to be about 50% lower with associated yield strains of about 0.06. For both nanorods, plastic deformation was found to proceed *via* slip in the {001} plane with direction $\langle 110 \rangle$ – a primary slip system for crystals with the fluorite structure. Dislocation evolution for the nanorod oriented along [110] was nucleated *via* a cerium vacancy present at the surface. A nanorod oriented along [321] and comprising twin-grain boundaries with {111} interfacial planes was calculated to have a yield strength of about 10 GPa (compression and tension) with the grain boundary providing the vehicle for plastic deformation, which slipped in the plane of the grain boundary, with an associated $\langle 110 \rangle$ slip direction. We also predict, using a combination of atomistic simulation and DFT, that rutile-structured ceria is feasible when the crystal is placed under tension. The mechanical properties of nanochains, comprising individual ceria nanoparticles with oriented attachment and generated using simulated self-assembly, were found to be similar to those of the nanorod with grain-boundary. Images of the atom positions during tension and compression are shown, together with animations, revealing the mechanisms underpinning plastic deformation. For the nanochain, our simulations help further our understanding of how a crystallising ice front can be used to ‘sculpt’ ceria nanoparticles into nanorods *via* oriented attachment.

^aDept. Engineering and Applied Science, Cranfield University, Defence Academy of the United Kingdom, Shrivenham, SN6 8LA, UK. E-mail: d.sayle@cranfield.ac.uk

^bAdvanced Materials Processing and Analysis Center, University of Central Florida, Orlando, FL-32816, USA

^cNanoScience Technology Center, University of Central Florida, Orlando, FL-32816, USA

^dMechanical Materials and Aerospace Engineering, University of Central Florida, Orlando, FL-32816, USA

^eDept. of Chemistry, University of Bath, Claverton Down, Bath, Avon, BA2 7AY, UK

^fNanoLAB Centre, Dept. of Materials Science and Engineering, Sheffield University, Sheffield, S1 3JD, UK

† Electronic supplementary information (ESI) available: Mechanical deformation of (a) ceria nanorod and (b) nanochain under compression. Calculated Radial Distribution Function associated with the unstrained and strained (comprising rutile polymorph) CeO₂[110] nanorod, compared to the RDF associated with the amorphous CeO₂ precursor. See DOI: 10.1039/c0nr00980f

Introduction

Ceria, CeO₂, is currently enjoying an expansion of applications, including: catalysis,¹ biomedicine,² fuel cell,³ sensor,⁴ chemical mechanical planarization⁵ and even as additives for rocket motors and energetic formulations.⁶ Moreover, the synthesis of ceria nanostructures has enabled researchers to exact profound changes over its (physical, chemical and mechanical) properties compared to the bulk parent material with important and wide ranging consequences for the applications enjoyed by this material.⁷ Central to the many applications of nanoceria is the mechanical durability of the material in response to for example, friction and wear, mechanical stress, thermal stress and mechanical/thermal fatigue. However, the mechanical properties of nanoceria are known to be different from the parent (bulk) material.⁸ In particular, it is well known that dislocations play a pivotal role with respect to mechanical strength. However, for

size-limited single crystals, as one traverses to the nanometre scale, dislocation nucleation becomes increasingly difficult enabling materials to deform near their theoretical strength limits⁹ facilitating ultra-strong materials. Suresh and Li acknowledge that ‘a lack of understanding of the deformation mechanisms that operate in ultra-strong materials severely limits our ability to create nanomaterials with the desired mechanical properties’.¹⁰

In addition to dislocations, other microstructural features[‡] can also play a pivotal role with respect to the mechanical properties. For example, nanopolycrystalline materials are more ductile compared to single crystals and can exhibit superplasticity *via* a grain-boundary sliding mechanism.¹¹ And while the mechanical properties of (nano)metals are receiving much attention, there are relatively fewer studies on ceramic nanomaterials; a review on the subject is provided by Zhu and Li.⁹

Measuring the mechanical properties of a nanomaterial is fraught with difficulty compared to the bulk parent material. For example, how does one hold and orient the material correctly? Nevertheless nanoscale ‘laboratories’ have been developed to replicate bulk mechanical testing, but at the nanoscale. Such laboratories have developed a variety of nanotools to undertake measurements including for example: microgrippers,¹² *in situ* mechanical deformation by nanoindentors¹³ and even nano-solder¹⁴ to weld nanomaterials together. Furthermore, the development of nanoscale tomography can now determine the nanostructure morphology and chemistry with three-dimensional spatial resolution.^{15,16} Clearly, the challenge experimentally is considerable and therefore atomistic computer simulation is ideally suited to provide complementary information. To this end we use atomistic simulation to explore the mechanical properties of ceria nanorods.

A key challenge in simulating the mechanical properties of a nanorod is the ability to capture, within the model, the microstructural features as observed experimentally. The model can then be used to determine the effect of such features on the properties. In particular, Agrawal and co-workers found, using a combination of experiment and simulation, that the calculated mechanical strength of ZnO nanorods was higher compared with experimental measurements, which was attributed to the microstructure.¹⁷ In particular, MD simulations were used to predict: (i) a stress-induced phase transformation, as opposed to brittle failure (and no transformation) observed experimentally, and (ii) fracture strains in the range 6.5–7.5%; experimentally, fracture was observed to range from 2.4 to 6%. To account for these discrepancies, the authors argued that microstructural features, in this case surface defects, reduce the average nucleation stresses because of stress concentrations. Specifically, for the atomistic model to be used to predict properties that are sufficiently accurate or realistic to be of value to experiment, then the atomistic model, which is ‘normally pristine’, needs to include (microstructural) features that will likely influence the particular property they are simulating. On the other hand, in the same paper, the simulation delivered unique understanding to explain that the brittle fracture, observed experimentally, might be attributed to the very high strain rate at the point of fracture. In

particular, they argued that the nanodevice was not able to respond quickly enough to reduce the strain as the material fractured. Clearly, simulation can provide unique and sometimes profoundly unexpected insights to help complement and interpret experiment.

If atomistic simulation is to help experiment by reliably predicting behaviour and properties, then the atomistic model must include the rich variety of microstructural features observed experimentally. Here, we address this issue and generate atomistic models of ceria nanorods, which comprise microstructural features observed experimentally. These include: morphology of the nanorod—surfaces exposed, steps, edges corners; nanorods comprising isolated and associated point defects and voids; nanorods aligned along different axes; nanorods comprising grain-boundaries and nanochains comprising an assembly of (structurally resolved) nanoparticles, which include dislocations. The mechanical properties are then simulated using these atomistic models to help understand how the microstructural features influence or indeed govern the mechanical behaviour.

To introduce microstructural features into an atomistic model is difficult, for example see ref. 18. Accordingly, we argue that the easiest way of introducing such complexity is to attempt to simulate the experimental strategy used to fabricate the material. We identify two driving mechanisms: crystallisation¹⁹ and the self-assembly of nanoparticles,²⁰ which are used to help guide our simulation strategies for generating the atomistic models.

Methods

In this section we outline the potential model used to describe the ceria nanorods; the computer code used to perform the molecular dynamical simulations; the approach to generating a fully atomistic model of a ceria nanorod, which comprises a complex microstructure; the mechanism for performing the simulated deformation under uniaxial loading and unloading and finally the computational details of DFT calculations.

Potential model

All calculations, presented in this study, were based upon the Born model of the ionic solid, where the energy, E , of the system is given by:

$$E(r_{ij}) = \sum_{ij} \frac{Q_i Q_j}{4\pi\epsilon_0 r_{ij}} + \sum_{ij} A \exp\left(\frac{-r_{ij}}{\rho}\right) - Cr_{ij}^{-6}$$

the first term represents the Coulombic interaction between ion i of charge Q_i and ion j of charge Q_j , which are a distance r_{ij} apart. The second term is of the Buckingham form, which is particularly effective in representing ionic solids. Model parameters,²¹ used to describe CeO₂, are presented in Table 1. These parameters were fitted to experimental data and therefore the hypersurface they describe is generally most accurate in the vicinity of the fit. Normally, as was the case for ceria, the parameters were fitted to the low-temperature (perfect) crystal structure. Accordingly, at interatomic separations away from equilibrium distances, the potential model may prove less reliable.²² Clearly, to have confidence in the results, the potential model is required to accurately represent the ceria at interionic separations, which differ from the low-temperature equilibrium values.

[‡] This includes for example grain-boundaries, morphology and surfaces exposed, isolated and associated point defects.

Table 1 Interionic potential parameters, of the form: $E(r_{ij}) = \sum_{ij} \frac{Q_i Q_j}{4\pi\epsilon_0 r_{ij}} + \sum_{ij} A \exp\left(-\frac{r_{ij}}{\rho}\right) - Cr_{ij}^{-6}$, used to describe the ceria nanorods

Atom <i>i</i>	Atom <i>j</i>	<i>A</i> /eV	$\rho/\text{\AA}$	<i>C</i> /eV \AA^6	Cut-off/ \AA
O	O	22764.30	0.149	27.89	10.0
O	Ce	1986.83	0.351	20.40	10.0
Ce	Ce	Set to zero			
Atom	Mass/amu		Charge/e		
O	16.00		−2.0		
Ce	140.12		+4.0		

A particularly exacting test of how accurately the force field maps the potential hypersurface is to simulate the crystallisation of a nanoparticle starting from a molten precursor. In particular, previously we showed that a molten ceria nanoparticle crystallises into a polyhedral nanocrystal in quantitative agreement with the experiment.⁵ Specifically, the simulation yielded the structure of a crystalline seed, which spontaneously evolved and nucleated the amorphous nanoparticle into a nanocrystal. Moreover, the polymorphic structure, morphology and surfaces exposed were correctly generated, from an amorphous precursor, during the simulation. We note that during an amorphous–crystalline phase change simulation, bond distances deviated considerably (over 10%) from the perfect crystal.²³ This study showed that the potential model is capable of simulating accurately the dynamical behaviour of ceria across a broad region of the potential hypersurface, including a phase transformation.

We also note that the O–O potential used in this study was not derived specifically for ceria; rather this transferable potential was derived against a range of metal oxides and has been successfully used to model a variety of oxides.²⁴ The ceria potential has been used extensively over the past twenty years to model: nanorods,²⁵ nanotubes²⁶ and for calculating important properties including oxygen mobility²⁷ and defect formation energies.²¹ Accordingly, we argue that the potential model describes accurately the hypersurface for a broad range of interatomic distances and is therefore well suited to this present study proffering more confidence in the prediction of the remarkable elastic properties and phase change associated with a ceria nanorod.

Simulation code

The DL_POLY code was used to perform all the molecular dynamics (MD) simulations;²⁸ the user manual provides comprehensive analytical descriptions and discussion of the molecular dynamics simulations, force fields, boundary conditions, algorithms and parallelisation methods used in these simulations.

Three-dimensional periodic boundary conditions were used to represent the nanorod, which repeats infinitely along the length of the rod. Specifically, the rod has neither a head nor tail and the simulation is performed on a periodic array of parallel rods. The size of the periodic repeat, perpendicular to the rod, needs to be chosen carefully to balance computational cost, yet minimise artificial interactions between its periodic neighbours. Here, we

chose a value of 9.6 nm and the periodic repeat along the length of the rod was also 9.6 nm. We note that the (short) length of the nanorod might impart some mechanical stability in that it prevents the rods from buckling.

Atomistic model generation

In this section we describe how the atomistic models for the ceria nanorods and nanochain were generated. All images presented in this study are representations of the atom positions comprising full atomistic models and are not schematics. Molecular graphics were performed using VMD²⁹ and Materials Studio.

Ceria nanorod oriented along [110]. To generate a ceria nanorod, a ‘cube’ of CeO₂, comprising 15 972 atoms (5324 Ce, 10 648 O), was cut from the parent material and the system melted by applying constant volume MD simulation at high temperature (8000 K); the simulation cell size was sufficiently large to ensure that the nanoparticle does not feel any (repulsive or attractive) interaction from its periodic neighbours (Fig. 1(a)). The size of the simulation cell was then reduced in one dimension to enable the nanoparticle to interact and agglomerate with its periodic neighbours (Fig. 1(b)).¹⁹ MD simulation, performed on the system for 1000 ps at 8000 K, facilitated the evolution of the nanorod (Fig. 1(c)). The nanorod was then crystallized by performing MD simulation at 3750 K to yield a nanorod with [110] as its principle axis. Simulated crystallization was performed for sufficient duration to converge the energy—typically 2 ns.

Ceria nanorod oriented along [211]. To generate a model atomistic structure for a ceria nanorod with a principle axis along [211] a method identical to that used to generate a ceria nanorod with [110] principle axis was employed. However, rather than crystallising the system at 3750 K, crystallisation was performed at 3400 K, which resulted in the evolution of a nanorod oriented along [211].

Ceria nanorod with grain-boundary. To generate a nanorod that comprises a grain-boundary traversing its structure, simulated crystallisation, starting from the amorphous precursor, Fig. 1, was used. However, as the system crystallises, two seeds must spontaneously evolve within the amorphous sea of ions comprising the nanorod. In particular, as the crystallisation fronts emanating from each (necessarily misoriented) seed impinge upon one another a grain-boundary evolves. Typically, a nanorod comprising two misoriented grains was achieved by performing the crystallisation step several times at very slightly different temperatures and molecular graphics used to observe whether two seeds evolve within the same system. We note that by changing the crystallisation temperature by only 5 K can lead to a significantly different structure; experimentally when one synthesises nanorods of ceria, the nanorods are never identical even though they are synthesised at the same time under identical conditions. Indeed, by simulating crystallisation, the method is able to capture subtle structural variations analogous to the experiment. Here, a crystallisation temperature of 3250 K was used to facilitate evolution of the grain-boundary.

The crystallisation of the nanorod, which comprises a grain-boundary, is shown in Fig. 2. In particular, at the start of the

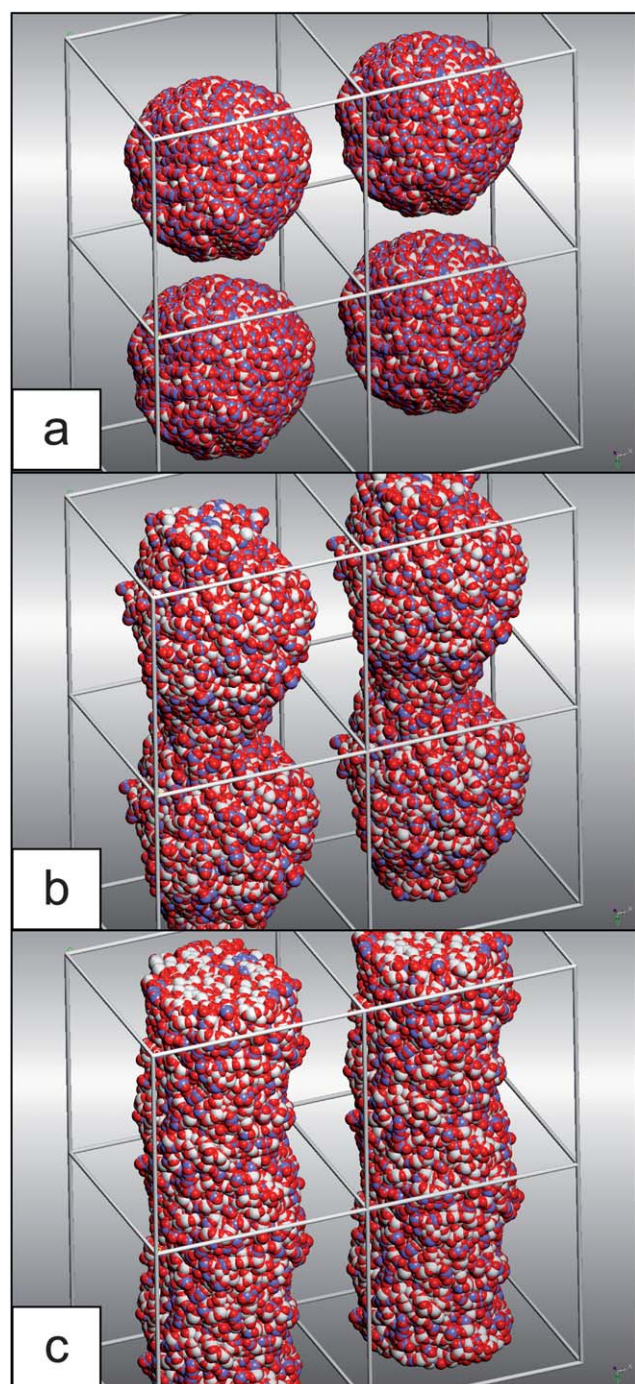


Fig. 1 Strategy used to generate atomistic models for the ceria nanorods. (a) Amorphous nanoparticles of ceria are positioned into a simulation cell. (b) Nanoparticles agglomerate together (c) final structure of the amorphous nanorods. Cerium is coloured white and oxygen, red. Blue atoms correspond to oxygen ions originally at the surface, which help reveal the considerable mobility of the ions.

simulation an amorphous nanorod is observed, 2(a), which under MD simulation evolves spontaneously a crystalline seed, 2(b), conforming to the fluorite structure, 2(c). A second fluorite-structured crystalline seed is then observed to evolve and under MD simulation each seed nucleates the crystallisation of the

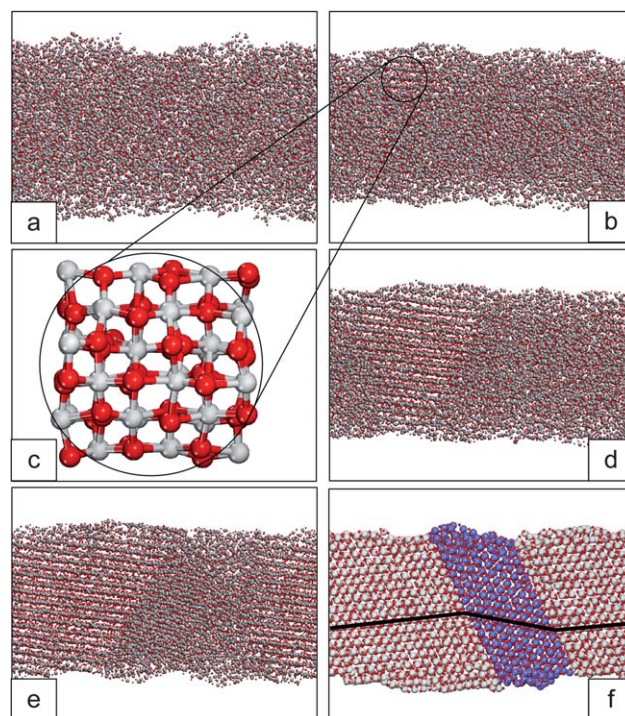


Fig. 2 Crystallisation of a nanorod at 3250 K, which evolves a grain-boundary. (a) At the start of the simulation; (b) after 1100 ps; (c) segment cut from (b) revealing that the ceria has crystallised into the fluorite structure; (d) 1400 ps; (e) 1600 ps; (f) 2000 ps, here a slice is cut through the nanorod to reveal more clearly the grain-boundaries.

remaining amorphous sea of (Ce, O) ions, 2(d) and (e). Finally, at the end of the simulation, a model for a nanorod, which includes two grain-boundaries traversing through the structure is generated, 2(f). Inspection of the nanorod revealed that the grain boundaries are twins with principle axis similar to $\{321\}$ and $\{111\}$ interfacial planes. In particular, the nanorod comprises a twinned grain with two grain-boundaries.

Ceria nanochain. To generate a nanochain, four (amorphous) nanoparticles of CeO_2 , each comprising 6144 atoms, were introduced, equally spaced, into a simulation box $13 \times 13 \times 13$ nm in size. Constant volume MD simulation was performed at 3200 K for 6800 ps. Under MD simulation the nanoparticles crystallise; nucleating seeds spontaneously evolved in each of the CeO_2 nanoparticles. As the nanoparticles crystallised, they moved closer together; the nanoparticles were observed to be attractive to one another and (oriented) attached at $\{111\}$, $\{110\}$ and $\{100\}$ faces. This is in full accord with experiment, where CeO_2 nanoparticles, 4 nm in diameter are perfectly aligned and epitaxially fused together *via* $\{111\}$ or $\{200\}$.³⁰

Two attached nanoparticles are shown in Fig. 3(a). We note that the nanoparticle, coloured green, comprises a dislocation with screw character, highlighted by the arrow, which traverses through the nanoparticle. Upon prolonged MD simulation, the dislocation anneals out to enable alignment of the atomic planes of the two nanoparticles, 3(b). The interfacial plane of two nanoparticles, which have attached at $\{111\}$ are shown in 3(c). Nanoparticles, attached at $\{100\}$ are shown in Fig. 3(d) and (e). During the MD simulation the nanoparticles reorient,

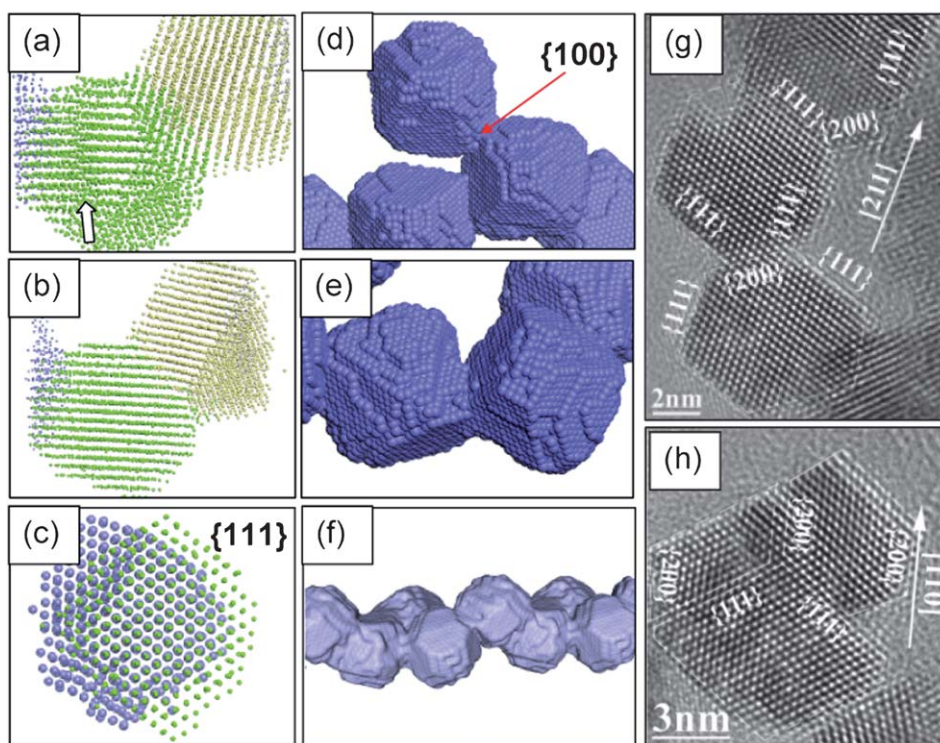


Fig. 3 Generating atomistic models for nanochains *via* the simulated self-assembly of polyhedral ceria nanoparticles; (a) nanoparticles, which include a dislocation (arrow); (b) the dislocation is annealed out; (c) oriented attached nanoparticles revealing the coherent interfacial planes, viewed along $\langle 110 \rangle$; (d) nanoparticles attached at $\{100\}$; (e) $\{100\}$ attachment with rotation; (f) final structure of the nanochain comprising oriented attached nanoparticles. HRTEM images to compare with the atomistic models: (g) nanoparticles attached at $\{200\}$ and (h) nanoparticles attached at $\{111\}$ reprinted with permission from ref. 30 Copyright 2007 American Chemical Society.

presumably to facilitate a better match between the faces of the truncated octahedral nanoparticles. The final structure of the nanochain is shown in 3(f). Experimentally, truncated octahedral ceria nanoparticles have been observed to attach *via* both $\{111\}$, and $\{100\}$, Fig. 3(g) and (h), which helps validate our atomistic models; a review on oriented attachment is found in ref. 31.

Deformation simulation. The mechanical properties were calculated by equilibrating the systems to the target temperature by performing constant pressure MD simulation at 300 K for 100 ps with 25 ps equilibration, prior to simulating strain, which was achieved by sequential scaling of the atom coordinates and performing constant volume MD simulation at 300 K using a Nosé–Hoover thermostat;³² a strain rate of about 10^7 s^{-1} was attained. Deformation simulations using this strategy have been performed previously.²⁵

Ab initio calculations. All the calculations were performed using the VASP code.^{33,34} The valence electronic states are expanded in a basis of plane waves, with the core–valence interaction represented using the projector augmented wave (PAW) approach.^{35,36} The frozen core is [He] for oxygen and [Xe] for cerium. The exchange–correlation functional applied is the Perdew–Burke–Ernzerhof (PBE) GGA.³⁷ We also include the Hubbard–U term using the methodology of Dudarev,^{38,39} which enables us to account for the presence of the localized Ce(III) states. However, this approach suffers from a strong dependence

on the choice of the value of the U parameter. The sensitivity of the results to the value of U for GGA + U calculations of ceria has been discussed elsewhere.⁴⁰ For our calculations a value of 5 eV for U was used for the f orbitals of Ce. 3D periodic boundary conditions were used throughout the calculations. The cut-off energy for the plane wave basis is 500 eV, and the Brillouin zone was sampled using $4 \times 4 \times 4$ and $4 \times 4 \times 6$ Monkhorst Pack grids for cerium dioxide in the fluorite structure and in the rutile structure, respectively.

The approach we adopted to investigate whether cerium dioxide might exhibit the rutile structure, while under tension, was by applying the zeroth order common tangent construction to evaluate the pressure at which the two phases are in equilibrium. We also calculated the hydrostatic pressure. In particular, we first found the geometry optimised bulk rutile structure. The symmetry was then held fixed and the cell volume was allowed to change during minimization. The energy and pressure of the fluorite-structured material, having the same cell volume per cerium unit as the rutile phase, were then calculated. This represents the pressure at which the fluorite structure has the same volume as the un-strained rutile phase.

Results

In this section we consider the atomistic structures and mechanical properties of each of the three nanorods and nanochain.

Atomistic structure

The nanorod oriented along [110] is shown in Fig. 4(a) and reveals that the rod exposes predominantly {111} and {100} facets and comprises a hexagonal cross-section in accord with the experiment.⁴¹ Exposure of {111} is not surprising, because $\text{CeO}_2(111)$ is the most stable surface.²¹ Conversely, $\text{CeO}_2(100)$ is dipolar⁴² and therefore a mechanism for quenching the dipole to stabilise the surface is needed. Close inspection of {100} reveals that half the oxygen ions from the top layer are vacant to give a stoichiometry of CeO rather than CeO_2 , which quenches the dipole. We note that this process was found to occur dynamically during crystallisation. The existence of CeO_2 {100} is well documented experimentally for ceria nanomaterials,⁷ and the structural changes required to quench the dipole are correctly predicted in our atomistic models for the nanorods. The atomistic model for the nanorod oriented along [211] is shown in Fig. 4(b) and, similar to the CeO_2 nanorod oriented along [110], comprises {111} and {100} facets. The atomistic model of the nanorod, which comprises a grain-boundary is shown in Fig. 4(c) and the nanochain in Fig. 4(f), the latter is compared to the experiment in 4(g).⁴³ We note that all nanorods comprise

a variety of microstructural features including surface steps and isolated and associated defects such as Ce and O vacancies.

Nanorods oriented along [110] have been synthesised⁴¹ and are reproduced in Fig. 4(d). Nanorods oriented along [211] have also been observed,³⁰ Fig. 4(e). Here, the authors used oriented attachment of truncated octahedral nanoparticles. Specifically, the authors found that nanoparticles attached at {100} facets facilitate the formation of nanorods aligned along [211], conversely attachment at {111} facilitates nanorods aligned along [110].

Mechanical properties

In this section we present the calculated mechanical properties, derived from stress–strain curves using the model nanorods and nanochain, and the mechanisms associated with elastic and plastic deformation and fracture. Simulated stress–strain curves are shown in Fig. 5 and the mechanical properties, including strength, yield points and elastic moduli for each nanorod, derived from the stress–strain traces, are given in Table 2. Calculated values of the bulk modulus and elastic modulus for the parent bulk material are 261 and 453 GPa respectively.

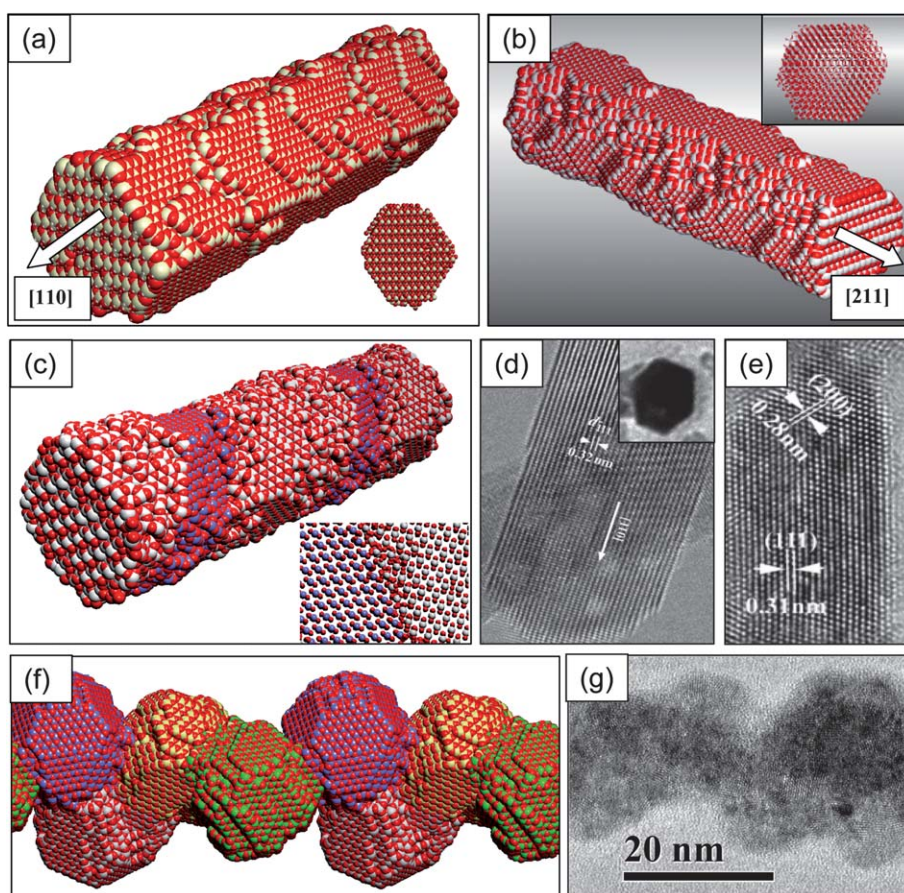


Fig. 4 Atomistic models for the three nanorods and nanochain compared with experiment. (a) Nanorod oriented along [110]; (b) nanorod oriented along [211]; (c) nanorod, which comprises twin grain-boundaries; (d) HRTEM of a nanorod with growth direction along [110] taken from ref. 41; (e) HRTEM of a nanorod with growth direction along [211] reprinted with permission from ref. 30 Copyright 2007 American Chemical Society; (f) atomistic model for the ceria nanochain; (g) HRTEM of the ceria nanochain. Cerium is coloured white and oxygen is red. In (c) the cerium in the grain boundary region is coloured blue for clarity; for the nanochain, (f), cerium is coloured blue, yellow, green and white to help distinguish the component nanoparticles.

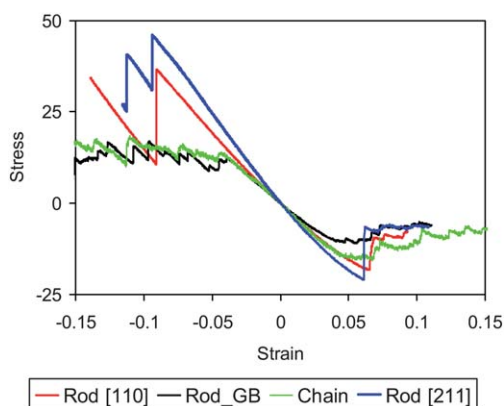


Fig. 5 Stress–strain curves calculated for the three ceria nanorods and nanochain.

Deformation mechanism. In this section we examine the atomistic models as they respond to tensile and compressive strains in an attempt to determine the mechanisms underpinning elastic and plastic deformation and fracture.

Nanorods oriented along [110] and [211]. Tension induced deformation of the perfect ceria nanorods, with principle axes [211] and [110], is shown in Fig. 6. For the nanorod oriented along [211] the rod expands elastically up to a strain of 0.06 and then fractures; images showing the nanorod just before (strain 0.061) and after (strain 0.062) fracture are shown in Fig. 6(a) and (b) respectively. The nanorod fractures to yield {111} surfaces, Fig. 6(c), which is energetically the most stable surface of ceria. Conversely, the nanorod oriented along [110], does not fracture; rather it undergoes a fluorite-to-rutile phase change, Fig. 6(d).²⁵

The electronic structure simulations, as well as providing a test for the interatomic potentials, supply further evidence supporting the prediction of our potential model that cerium dioxide can undergo a fluorite-to-rutile phase change. Table 3 lists the lattice parameters of rutile- and fluorite-structured CeO₂ having the same volume per cerium unit, the relative energy of the structure per cerium unit and the hydrostatic pressure calculated with DFT-GGA and GGA + U and potential-based technique. The lattice parameters and the energy of the fluorite structure at zero pressure as well as the equilibrium transition pressure obtained from the slope of the zeroth order common tangent are listed for both DFT and potential-based technique.

The comparison between the energies of rutile- and fluorite-structured CeO₂ per cerium unit, calculated using DFT, reveals

that the rutile phase is energetically *more* stable compared to the fluorite phase by 0.14 eV (GGA) and 0.28 eV (GGA + U) during tension as predicted by the potential model. The results of the zeroth order common tangent construction, where the phases will be at equilibrium gives equilibrium pressures under tension of −6.7 GPa (DFT), −7.1 GPa (DFT + U) and −12.5 GPa (potential model). Given the small energy differences as well as neglect the thermal effects shows good agreement between the two approaches. Indeed the difference in energies between the potential based simulations and DFT calculations for fluorite/rutile polymorphs is within 0.15 eV per Ce unit of each other, which is comparable with the energy differences calculated using the different flavours of DFT. The mechanism for the conversion to rutile is based on the removal of the tension acting on the rod, and may not be under total equilibrium conditions, so as a way of estimating the extent of the pressure range where the transition may occur we considered the hydrostatic tension of the fluorite phase at the volume for the rutile phase when the tensile stress is completely removed. At this point the stress corresponds to −19.7 GPa (GGA) or −18.8 GPa (GGA + U) and −26.7 GPa with potential based calculations, using METADISE⁴⁴. The tension induced fluorite-to-rutile phase transformation was calculated to occur at a stress of about −18 GPa in the nanorod aligned along [110] (Fig. 5). This value fits into the pressure range, and particularly considering the additional components in the rod, over temperature, microstructure and large surface area the agreement is in good accord. Perhaps equally significant is that the DFT predicts a much lower transition pressure, which may point to the formation of the new phase grown under experimental conditions appearing at lower pressures than predicted *via* the simple, but robust, interatomic potential. Corroboration between the atomistic modelling and DFT increases the confidence that such a transformation might exist and therefore may be observed experimentally in the future.

The atomistic behaviour of the CeO₂ nanorod, oriented along [110], under compression at the yield point is shown in Fig. 7. The deformation mechanism is dislocation driven: specifically a dislocation, D1, emanates at the bottom surface of the rod, Fig. 7(a), at the site of a cerium vacancy, which appears to nucleate the dislocation. A second dislocation, segment D2, also nucleates on the other side of the nanorod. Under increasing compression, D1 traverses into the bulk of the nanorod in the direction of the arrow, 7(d), and finally emerges at the other side of the nanorod, 7(e). This process then repeats resulting in a second atomic layer protruding out of the surface, forming a clear step 7(f) and (g). Lattice slip was observed within the

Table 2 Cross-sectional area, strength, yield point and elastic modulus, calculated for the three CeO₂ nanorods and the nanochain. *C* and *T* correspond to compression and tension respectively. The second number associated with the strength corresponds to the force calculated per individual nanorod or nanochain

	Area/nm ²	Strength/GPa, μ N		Yield point		Elastic modulus/GPa	
		<i>C</i>	<i>T</i>	<i>C</i>	<i>T</i>	<i>C</i>	<i>T</i>
Rod [211]	16	46, 0.7	−21, −0.3	−0.094	0.061	480	410
Rod [110]	20	37, 0.7	−18, −0.4	−0.091	0.066	380	340
Chain	7	13, 0.1	−15, −0.1	−0.045	0.046	320	340
Rod (GB)	20	12, 0.2	−10, −0.2	−0.039	0.047	320	320

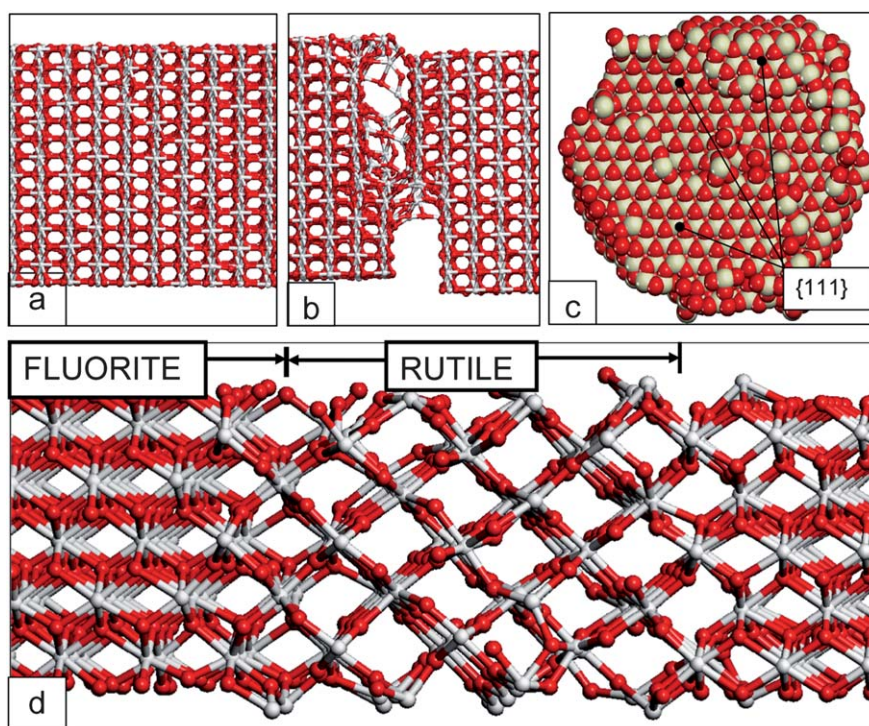


Fig. 6 Structure of the CeO_2 nanorods, oriented along $[211]$ and $[110]$, under tension. (a) Nanorod oriented along $[211]$ just prior to fracture and (b) just after fracture. (c) Shows the fracture plane to be $\{111\}$. (d) Nanorod oriented along $[110]$, after a strain of 0.083 showing the (reversible) fluorite—rutile transformation.

$\{100\}$ plane with direction $\langle 011 \rangle$ —a primary slip system for crystals with the fluorite structure. Fig. 7(h) and (i) depict the glide of the $\langle 011 \rangle \{100\}$ dislocation associated with such plastic deformation of the nanorod. The stress–strain curve, with stress presented as a function of time, is shown in Fig. 7(j) and (k) and reveals that the dislocation travels at a speed of about 3000 ms^{-1} Fig. 7(c)–(e). An animation showing the dislocation moving through the nanorod at this speed is available in the ESI†. The nanorod oriented along $[211]$ also suffered plastic deformation, facilitated by slip in $\{001\}$ with $\langle 110 \rangle$ direction.

Nanorod with grain-boundary. The ceria nanorod, encompassing a twin-grain with parallel $\{111\}$ grain-boundaries at the start of the simulation prior to tension induced strain, is shown in Fig. 8(a); the locations of the $\{111\}$ grain boundaries are highlighted by the arrows. A $\langle 111 \rangle$ view of the two adjacent $\text{Ce}\{111\}$

planes at the boundary, indicated by the blue arrows, is shown in Fig. 8(b) and is enlarged in 8(c). Inspection of the nanorod under tensile strain reveals that the nanorod first slips by a twinning dislocation along this grain boundary (blue arrows) resulting in a decrease in the size of the twin-grain. This is demonstrated by the relative positions of Ce atoms in the two adjacent $\text{Ce}\{111\}$ planes at the grain-boundary (blue), before (strain 0.0480) and after (strain 0.0483) slip, as shown in Fig. 8(d) and (e) respectively. The nanorod then shears along the second grain boundary (red); the inset, Fig. 8(a) shows the final structure of the nanorod after a strain of 0.11; the strains can be usefully correlated to the stress–strain curve, Fig. 5.

The images in Fig. 9 show the nanorod with grain-boundary under compression as a function of time. Inspection of the images, reveals that the nanorod fails (*via* slip) along $\langle 110 \rangle$ in the plane of the grain-boundary— $\{111\}$; the nanorod suffers

Table 3 Lattice parameter, volume, energy per cerium unit and hydrostatic and equilibrium transition pressure of rutile- and fluorite-structured CeO_2 calculated using DFT and potential-based techniques

	Structure	Lattice parameters/ \AA		$V/\text{\AA}^3$	Energy/eV	Pressure/GPa	Equilibrium transition pressure/GPa
		$a = b$	c				
DFT-GGA	Rutile	5.1445	3.6268	47.99	−25.87	0.0	−6.7
	Fluorite	5.4622	5.4622	40.74	−26.24	0.0	
	Fluorite	5.7687	5.7687	47.99	−25.73	−19.7	
DFT-GGA + U	Rutile	5.1867	3.6319	48.85	−24.03	0.0	−7.1
	Fluorite	5.4887	5.4887	41.33	−24.44	0.0	
	Fluorite	5.8030	5.8030	48.85	−23.75	−19.8	
Potential-based	Rutile	5.0304	3.6070	45.64	−104.81	0.0	−12.5
	Fluorite	5.4292	5.4292	40.01	−105.31	0.0	
	Fluorite	5.6727	5.6727	45.64	−104.78	−26.7	

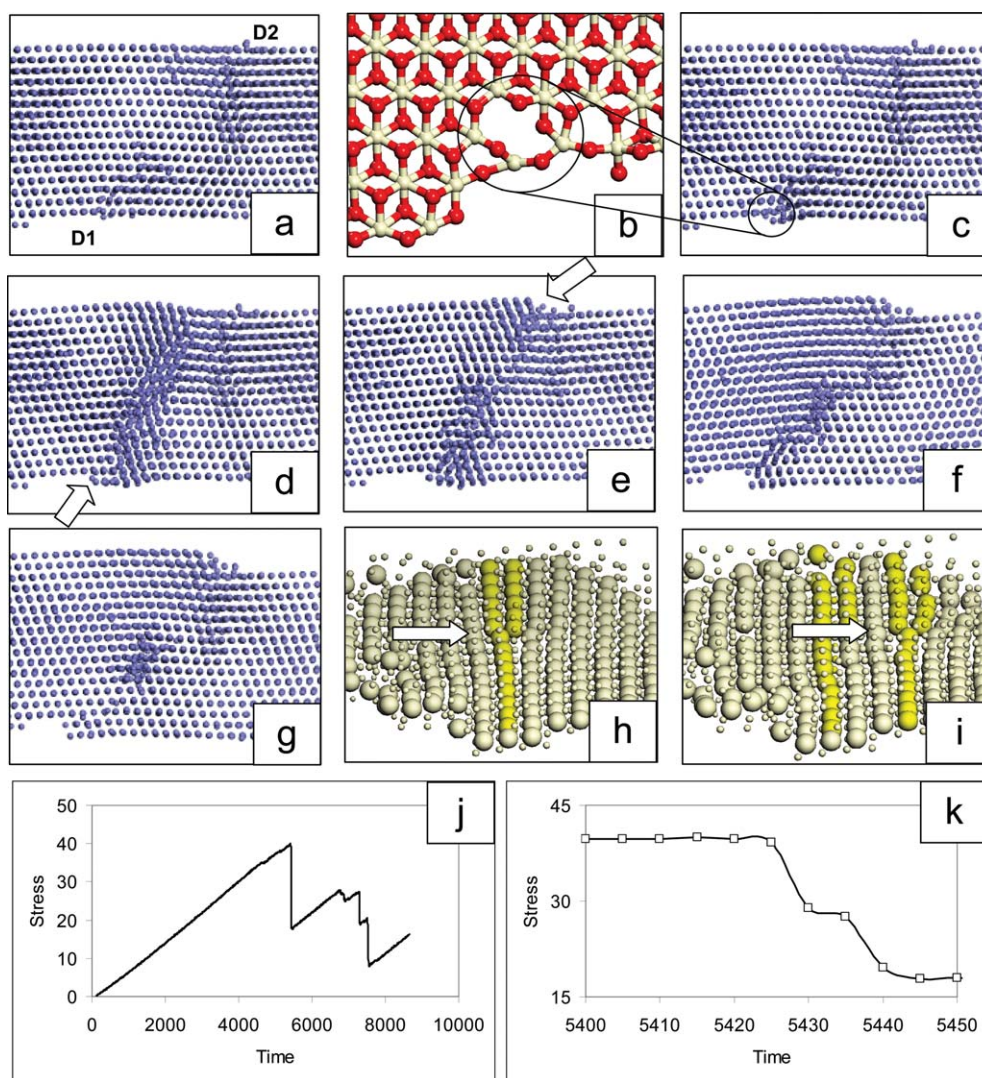


Fig. 7 Ceria nanorod, oriented along $[110]$, revealing the deformation mechanism under compression: (a) after 5319 ps (b) ball and stick model of the atom positions comprising the nucleating site before compression (cerium is white and oxygen is red); (c) 5427 ps; (d) 5427.5 ps; (e) 5428.5 ps; (f) 5442 ps; (g) 5631.5 ps; (h) and (i) show the cerium sublattice revealing dislocation glide from left to right; (j) stress–strain curve to correlate with atomistic models (k) enlarged segment of (j). Cerium is coloured blue; oxygen is not shown. Only a slice cut through the nanorod is shown to improve clarity.

repeated slip in the same plane. The stress–strain trace associated with this deformation, Fig. 5, reveals that the yield strength is reduced by about 75% compared to the nanorod (oriented along $[211]$), which does not include a grain-boundary, Table 2.

Nanochain. Compression and tension induced deformation of the nanochain are shown in Fig. 10 and 11 respectively. Under compression, the nanoparticles attached at $\{111\}$ slip along $\langle 110 \rangle$ and the coherent interface, Fig. 10(a), becomes mis-aligned, 10(b), culminating in a very poor match at about -0.11 strain, 10(c). We note that the slip is also associated with a slight rotation as evidenced in Fig. 10(a)–(c). Similarly, under tension, the nanoparticles attached at $\{111\}$, Fig. 11(a), suffer slip along $\langle 110 \rangle$, 11(b), and finally the nanoparticle fractures, 11(c). We note that the original interfacial plane between the adjoining nanoparticles remains after fracture, which occurs not at the interfacial plane, but rather deeper inside the (green) nanoparticle.

Nanochain under shear forces

Previously, we prepared ceria nanoparticles in aqueous solution and have shown the formation of nanorods *via* oriented attachment utilizing the templating effect of ice. The synthesis and physicochemical phenomena involved have been described in detail elsewhere.⁴³ In particular, we oxidized an aqueous solution of Ce(III) to Ce(IV) and subjected it to controlled freezing as the nanoceria crystals nucleate. Different morphologies of ceria nanoparticles were obtained as the water crystallizes into ice depending upon the duration of the freezing and the oriented attachment of nanoparticles. Specifically, as the water crystallises, the nanoparticles are forced into nanometre sized voids formed within the growing ice front. We theorised that the forces acting upon the nanoparticles, emanating from the crystallising ice front, compact the nanoparticles facilitating oriented attachment.

To explore the mechanism underpinning this transformation, we applied a (shear) force to one particular nanoparticle with

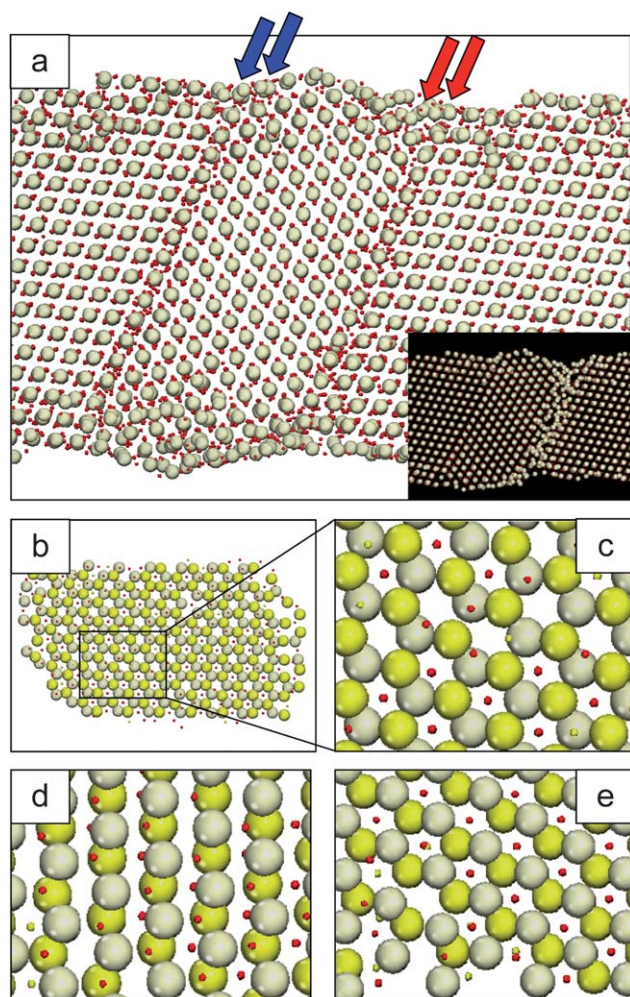


Fig. 8 CeO₂ nanorod, which comprises a twin grain with {111} grain-boundary, simulated under tension: (a) start of the simulation; (b) slice through the grain-boundary, viewed along $\langle 111 \rangle$, revealing the interfacial planes at the start of the simulation (c) enlarged segment of (b); (d) after 2350 ps; (e) after 2365 ps; (d) and (e) are viewed along $\langle 111 \rangle$ but with the white spheres to the front. The nanorod first slips along the first grain-boundary (blue arrows) and then fails along the second GB (red arrow); the final structure is shown as an inset in (a).

respect to another. Inspection of the behaviour as the nanochain deforms can be seen in Fig. 12; 12(a) shows the nanochain at the start of the simulation and 12(b), after a strain of 0.15. Fig. 12(c) shows the HRTEM images of freshly synthesized ceria nanoparticles. Aging the as-prepared ceria nanoparticles for 1 day subjected to subzero temperature led to formation of nanochains as shown in Fig. 12(d). We observed complete formation of ceria nanorods more than 1–2 μm long, shown in Fig. 12(e), after 2–3 weeks of aging. The high magnification image of nanorod in Fig. 12(f) reveals that the nanorods comprise individual ceria nanocrystals, 3–5 nm in size.

Inspection, using graphical techniques, of the behaviour of the model nanochain simulated under shear pressure reveals that the nanoparticles slide ‘over’ one another and are able to re-orient under the stress; we observe reorientation and attachment at {111}, {110} and {100}. The force required to exact such deformation was calculated to be about 0.1 μN . Accordingly, the

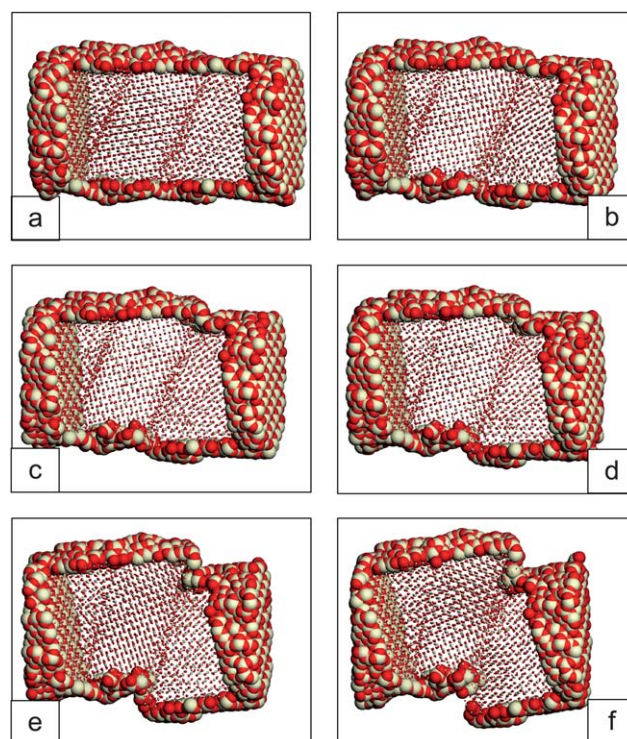


Fig. 9 Atomistic models of the Ceria nanorod, which comprises a grain-boundary, simulated under compression revealing that plastic deformation occurs *via* slip along the plane of the grain-boundary: (a) after 1250 ps; (b) 2500 ps; (c) 3750 ps; (d) 5000 ps; (e) 6250 ps; (f) 7500 ps. Two sizes of the spheres representing the atom positions have been used to improve clarity of the figure.

simulations support our previous hypothesis that the crystallisation of the ice exerts shear pressure upon the individual nanoparticles enabling them to re-orient and align at various faces to facilitate the straight edges of the nanorod; an animation showing the nanochain under compression is available in the ESI†.

In a related study, Lockwood and Inkson performed real-time direct imaging of the deformation of individual Si nanoparticle clusters under load. In particular, the study showed localized orientation changes in the individual Si nanoparticles during loading followed by fracture of the cluster along a weak interface between two nanoparticles within the cluster.⁴⁵ This supports the idea that loading can exact orientational changes upon individual nanoparticles. However, we propose that the chain comprising ceria nanoparticles did not fracture because the crystallization front of the ice forced the ceria nanoparticles into channels, which exact forces sufficient to compact them together. Specifically, we propose that any fracture of the individual nanoparticles would be quashed by forces crushing them together.

Discussion

By simulating the crystallisation process—similar to experiment—one is able to capture within the structural models all the (microstructural) features observed experimentally. This includes, morphologies and surfaces exposed, grain-boundaries,

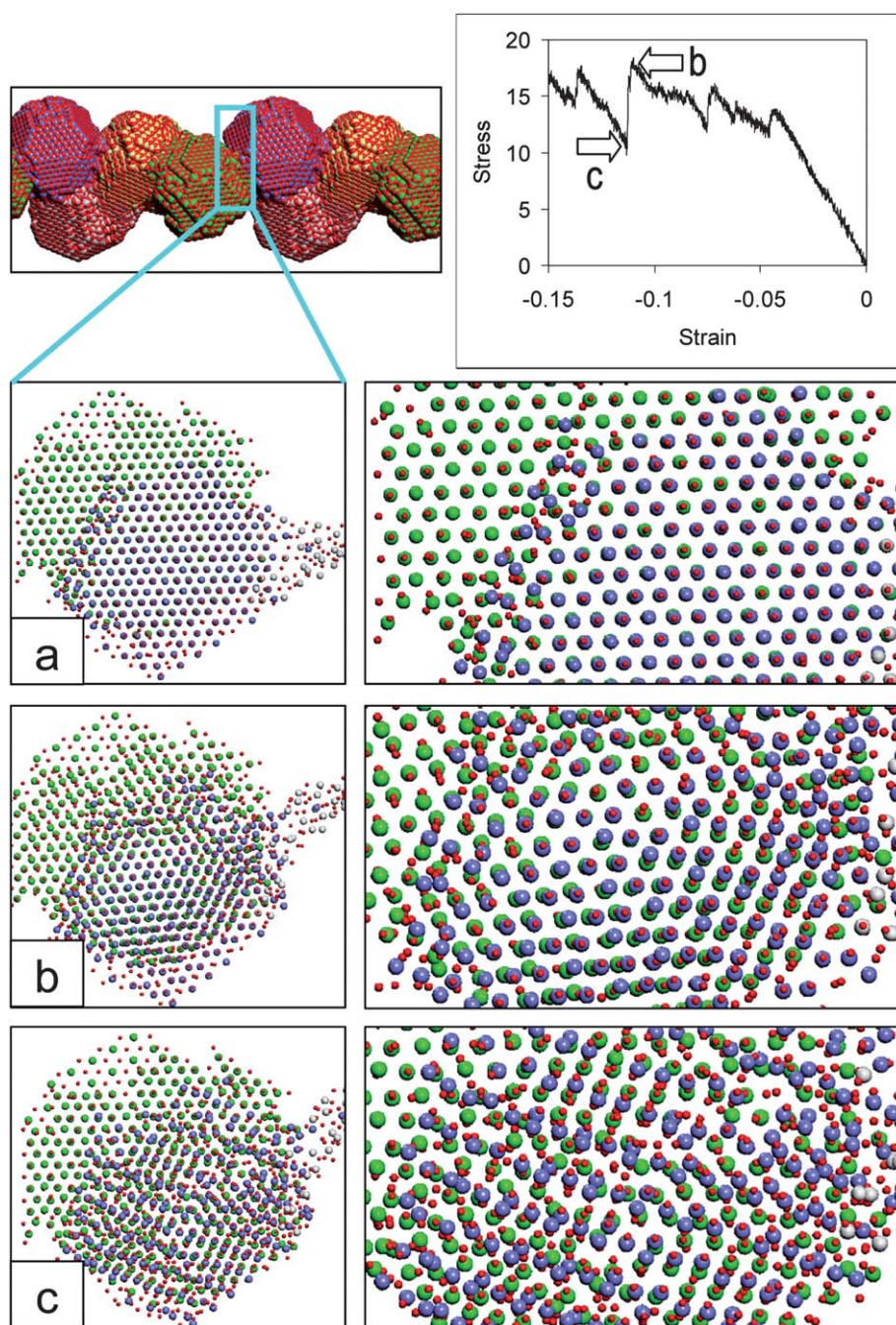


Fig. 10 Atomistic models of the ceria nanochain suffering plastic deformation under compression: Top left shows the atomistic model of the nanochain and top right, the stress–strain curve. (a) Start of the simulation; (b) after 5980 ps; (c) after 6105 ps. The interfacial plane is enlarged to the right of (a), (b) and (c) for clarity.

dislocations and point defects, and for the nanochain—the oriented attachment of the component nanocrystals. However, one is also exposed to the ‘random’ nature of crystallisation. In particular, it is difficult to facilitate the evolution of the nucleating seeds and the resulting microstructure is not easily controllable; rather significant trial and error—similar to experiment—is needed to facilitate models with desirable attributes. On the other hand simulated crystallisation enables a statistically realistic population of different structures to be generated. Further details pertaining to the method can be found in ref. 19.

Experimentally, direct measurements of oxide nanorods and nanotubes have recently been performed. In particular, Agrawal and co-workers¹⁷ measured the strength of ZnO nanowires and found that ‘the measured fracture strengths ranged from 3.33 to 9.53 GPa for nanowires with diameters varying from 20 to 512 nm, with brittle fracture at strains as high as 5%.’ The authors also comment upon the variability of experimental data and quote literature values for Young’s modulus ranging from 21–220 GPa, which exemplifies the experimental challenge associated with such measurements and reinforces the role that

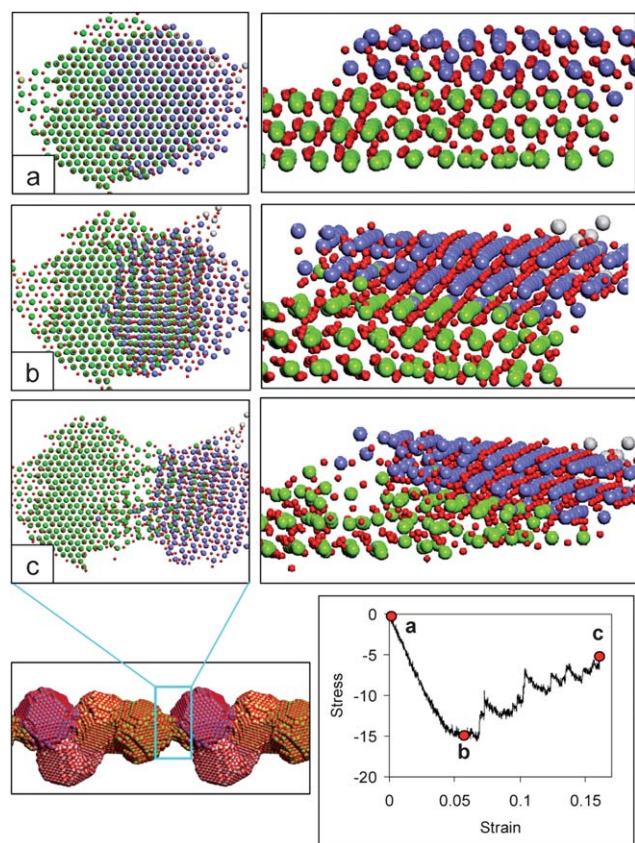


Fig. 11 Atomistic models of the ceria nanochain suffering tension-induced deformation: (a) start of the simulation; (b) after 3250 ps; (c) at the end of the simulation. The atomistic image of the nanochain (bottom left) is shown at the end of the simulation (strain = 0.17). The corresponding stress–strain curve is shown at the bottom right to correlate with the atomistic models. Plan views of the interfacial plane along which deformation occurs are shown to the left, and side views to the right.

simulation can play in helping elucidate the mechanical properties of nanomaterials. The authors also acknowledge that the predicted mechanical strength is higher compared to their experiments and proposed that surface defects might account for the lower strains to fracture measured experimentally. Accordingly, new models were generated, which included surface defects, and the simulations indeed revealed a reduction in strain to failure. Here, we find that the yield strength of a nanorod comprising a twin grain with $\{111\}$ grain-boundaries was about 70% less compared to a similar nanorod with no extended defect. Such simulations clearly demonstrate the pivotal role of microstructure on the mechanical properties of nanomaterials.

The nanorod oriented along $[110]$ under compression plastically deforms *via* slip conforming to $\{001\}\langle 110\rangle$. In particular, as the dislocation penetrates the surface it does so at a particular position on the surface of the nanorod. Inspection of this position revealed a cerium vacancy, which is energetically less stable compared to the pristine material. Accordingly, penetration of the surface at this position *via* a dislocation enabled a structural rearrangement effectively eliminating the defect. The vacancy thus acts as a nucleating site to help facilitate penetration of the dislocation at the surface. We propose that if the nanorod had been pristine at this position, the yield strength would have been

higher as it would have been energetically more difficult for the dislocation to penetrate the surface. Accordingly, we argue that the presence of such defects reduces the yield strength of the material. We note that immediately after penetration, the dislocation moved (at 3000 m s^{-1}) through the nanorod to emerge at the opposite side of the rod. The nanorod with $[211]$ growth direction also deformed plastically *via* slip conforming to $\{001\}\langle 110\rangle$. However, we note that the yield strength was 25% greater yet both nanorods were of similar diameter. This may be attributed to the area of the $\{001\}$ slip plane being significantly larger for the nanorod with $[211]$ growth direction and/or the vacancy, present at the surface of the nanorod with $[110]$ growth direction, facilitating a more facile deformation mechanism.

A concern with atomistic simulations using pair-potentials is that they may not be able to capture the behaviour of the material under high strain and large deviation from equilibrium bond distances from which they were derived. Here, we show that the fluorite–rutile phase change, predicted using pair-potentials of the Buckingham form were also ratified using density functional theory thus providing further evidence that pair potentials can indeed simulate the behaviour. Moreover, phase changes have also been predicted in nanorods under tension.^{46,25,17} In particular, Wang and co-workers predicted that ZnO nanorods undergo a phase transformation from wurtzite to BCT-4. They also predicted that the critical stress for nucleation, of the transformation and the elastic moduli decreased with the increase in the nanorod diameter. Moreover, the critical stress for the transformation decreased with increasing temperature. Shokuhfar and co-workers found that the Young's modulus of titanium dioxide nanotubes depends upon the diameter and wall thickness of the nanotube and is in the range of 23 to 44 GPa; nanotubes with 75 nm diameter and 5 nm thick walls collapsed at 1.0 to 1.2 μN during axial compression. We note that experimentally, 3 nm diameter ceria nanoparticles were stable up to pressures of 28 GPa and with no phase change to 65 GPa.⁴⁷ In exploring large strain plasticity of SiC nanowires Han and co-workers observed dislocation evolution starting at the surface.⁴⁸ We also observe dislocation evolution starting at the surface of the ceria nanorods under strain, Fig. 7. The correlation between experiment and simulation thus helps validate our methods and increases confidence that simulation can be used reliably to predict deformation mechanisms, which operate in nanomaterials.

Phase transitions in nanorods under tension have been reported using DFT. For example, Wang and co-workers used a combination of molecular dynamics and density functional theory to explore the behaviour of $[0001]$ oriented ZnO nanorods under mechanical stress and found a wurtzite to body centred tetragonal phase change when the stress increased above 7 GPa.⁴⁹ Similarly, Kulkarni and co-workers predict a wurtzite to a graphite-like ($P6_3/mmc$) hexagonal structure in $[01\bar{1}0]$ -oriented ZnO nanowires under uniaxial tensile loading.⁵⁰ Specifically, they found that the transformation was reversible with the ability to recover pseudoelastic strains up to 15%—a prediction that was subsequently confirmed experimentally in $[0001]$ oriented ZnO nanoplates and nanowires.

A rather intriguing study by Sangthong and co-workers revealed structural discontinuities with respect to the length of a nanorod.⁵¹ In particular, they used density functional theory to

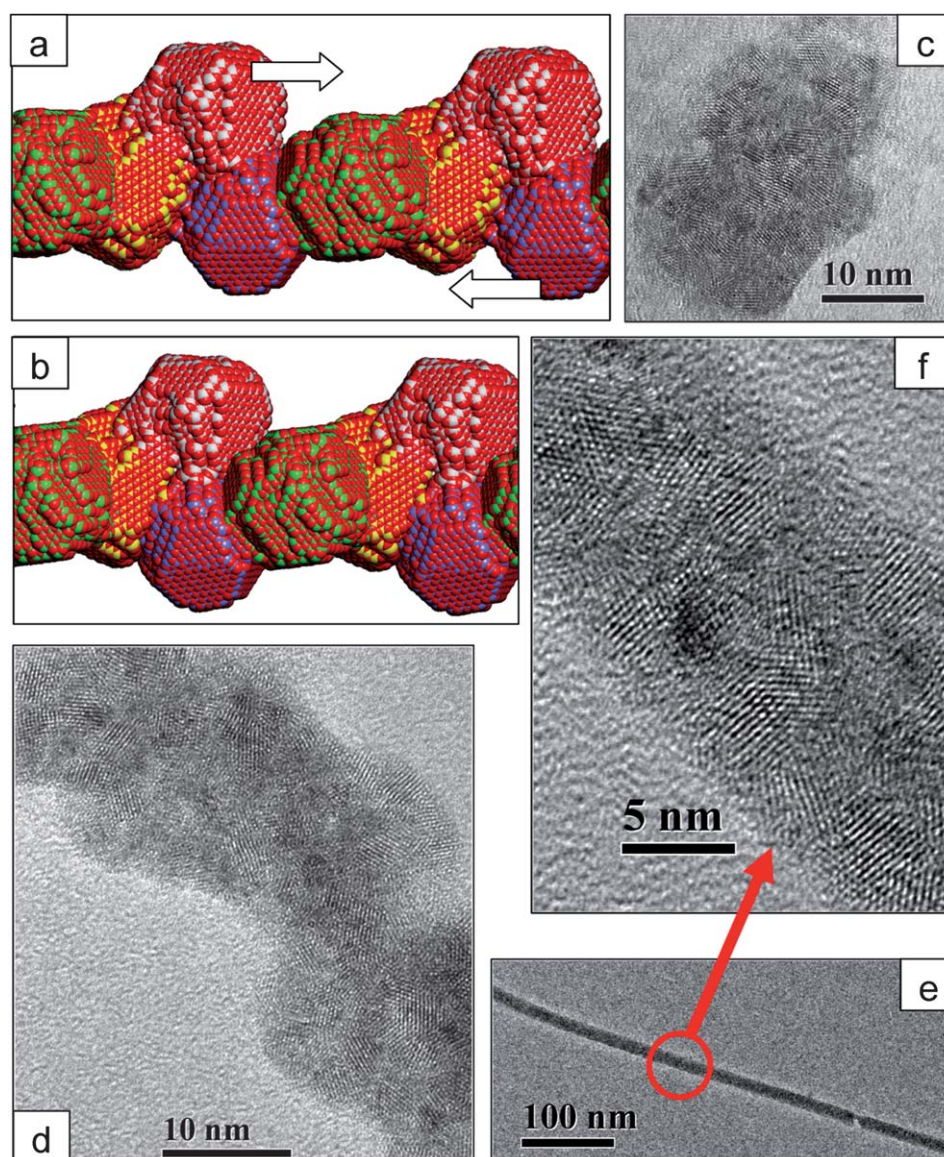


Fig. 12 Atomistic models of the ceria nanochain simulated under shear forces acting upon two nanoparticles within the ceria nanochain: (a) at the start of the simulation; (b) after a strain of 0.15; (c) HRTEM of individual CeO_2 nanoparticles (d) HRTEM image of 1 day old ice aged CeO_2 nanoparticles; (e) after ageing for 2 weeks in ice; (f) enlarged segment of (e) showing the individual crystallites comprising the nanorod.

explore the structure of CdS and CdSe particles and rods and found that ‘in ultra-thin nanorods—less than 10 nm in length—magic-cluster-based structures were calculated to be persistently energetically more favourable compared with wurtzite’. The authors also argue that the ‘length-dependent transition is also accompanied by a large change in the aspect ratio—a finding that could potentially be exploited in nano-mechanical transducers’. Analogous may perhaps be drawn between this behaviour and critical thicknesses (to structural modification such as dislocation evolution) and areas associated with supported thin films.

Predictions made by simulation that have been later confirmed experimentally demonstrate that simulation is now of sufficient maturity to be used predictively with respect to mechanical properties of nanostructures, which lends further support that the fluorite-to-rutile phase change might also be realized experimentally in the future.

The application of simulation to strained nanostructures is well placed to complement experiment to map phase space in areas where experimental measurement is difficult or indeed intractable at present. Accordingly, simulation can be used to help experiment locate areas of phase space that might prove advantageous. This may include, for example, identifying domains where the material undergoes changes in phase endowing the material with a wealth of new chemical, physical and mechanical properties, or identifying materials that can recover high elastic strains, which can, potentially, be exploited in (nano)energy storage.

Conclusion

The mechanical properties of a material are governed by its microstructure. Accordingly, if one is to use simulation to

provide predictions for experiment then it is necessary to capture such microstructural features within the atomistic model. Here, we use atomistic computer simulation to predict the mechanical properties of ceria nanorods and nanochains. Generating such models is not trivial, in particular, one needs the atomistic models to capture the growth direction of the nanorods, the surfaces exposed, and hence the cross-sectional shape, the presence of surface steps, edges and corners, isolated and associated point defects, dislocations and grain-boundaries all of which have been shown to impact significantly upon the mechanical properties. To facilitate such structures we have used simulated amorphisation and crystallisation and simulated self-assembly. In particular, experimentally, microstructure is introduced into a material during nucleation and crystal growth and therefore by simulating, in part, crystallisation we were able to introduce microstructural features, observed experimentally into the model.

Equipped with microstructural models, the mechanical properties were calculated. The results indicate that the single crystal nanorods were stronger than the nanorod, which comprised a twin grain with $\{111\}$ grain-boundaries. Moreover, the growth direction of the rod was found to play an important role; the rod oriented along $[211]$ was stronger compared to the nanorod oriented along $[110]$. The mechanisms for plastic deformation have also been explored: for nanorods without grain-boundaries or dislocations, the yield strength is high, but they eventually deform plastically *via* the evolution of dislocations resulting in slip conforming to $\{001\}$ $\langle 110 \rangle$. Conversely, for polycrystalline nanorods, the grain-boundaries provide the vehicles for plastic deformation; under compression or tension the nanorod slips along the plane of the grain-boundary.

For the nanorods with growth direction along $[110]$ we predict that under tension, the nanorod undergoes a fluorite-to-rutile phase change, which was not observed for nanorods with $[211]$ growth directions; rather the latter fractured with the evolution of $\{111\}$ surfaces. Using density functional theory we demonstrated that the fluorite-to-rutile phase change is feasible, which also further validates our potential model in reproducing such behaviour. However *ab initio* calculations do not explain the difference in the behaviour under tension of the two nanorods aligned along the $[110]$ and $[211]$ directions. Indeed, understanding the role of the different structural features (defects and morphology) and the rod growth direction play in this phenomenon is still a challenge.

For the nanochain, which comprises individual (oriented) ceria nanoparticles, a force acting upon the nanorod can influence the oriented attachment of the individual nanoparticles in the chain. We propose a mechanism to help explain how ceria nanorods, generated from nanoparticle pre-cursors are sculpted by the pressure exacted upon them during the crystallisation of the water in which they reside to form straight ceria nanorods. In particular, we calculate that a force of about $0.1 \mu\text{N}$ is required to reorient individual nanoparticles in the chain—such force provided by the crystallisation of the water.

Acknowledgements

EPSRC: GR/S84414/01, EP/H001220, EP/H001298, EP/H005838; NSF NIRT for nanoparticle work; Aquila (HPC at

Bath University <http://wiki.bath.ac.uk/display/HPC/Aquila>); Astral (HPC at Cranfield University). Seal acknowledges NSF International Travel Supplement to UK (CBET: 1028996) and NSF NIRT (CBET 0708172).

References

- 1 R. Di Monte and J. Kaspar, On the role of oxygen storage in three-way catalysis, *Top. Catal.*, 2004, **28**, 47–57.
- 2 S. M. Hirst, A. S. Karakoti, R. D. Tyler, N. Sriranganathan, S. Seal and C. M. Reilly, Anti-inflammatory properties of cerium oxide nanoparticles, *Small*, 2009, **5**, 2848–2856.
- 3 M. Mogensen, N. M. Sammes and G. A. Tompsett, Physical, chemical and electrochemical properties of pure and doped ceria, *Solid State Ionics*, 2000, **129**, 63–94.
- 4 E. Rossinyol, J. Arbiol, F. Peiro, A. Cornet, J. R. Morante, B. Tian, T. Bo and D. Zhao, Nanostructured metal oxides synthesized by hard template method for gas sensing applications, *Sens. Actuators, B*, 2005, **109**, 57–63.
- 5 X. D. Feng, D. C. Sayle, Z. L. Wang, M. S. Paras, B. Santora, A. C. Sutorik, T. X. T. Sayle, Y. Yang, Y. Ding, X. D. Wang and Y. S. Her, *Science*, 2006, **312**, 1504–1508.
- 6 D. L. Reid, A. E. Russo, R. V. Carro, M. A. Stephens, A. R. LePage, T. C. Spalding, E. L. Peterson and S. Seal, Nanoscale additives tailor energetic materials, *Nano Lett.*, 2007, **7**, 2157–2161.
- 7 X. W. Liu, K. B. Zhou, L. Wang, B. Y. Wang and Y. D. Li, Oxygen vacancy clusters promoting reducibility and activity of ceria nanorods, *J. Am. Chem. Soc.*, 2009, **131**, 3140–3141.
- 8 T. Brezesinski, J. Wang, R. Senter, K. Brezesinski, B. Dunn and S. H. Tolbert, On the correlation between mechanical flexibility, nanoscale structure, and charge storage in periodic mesoporous CeO_2 thin films, *ACS Nano*, 2010, **4**, 967–977.
- 9 T. Zhu and J. Li, Ultra-strength materials, *Prog. Mater. Sci.*, 2010, **55**, 710–757.
- 10 S. Suresh and J. Li, Deformation of the ultra-strong, *Nature*, 2008, **456**, 716–717.
- 11 V. Yamakov, D. Wolf, S. R. Phillpot, A. K. Mukherjee and H. Gleiter, Deformation-mechanism map for nanocrystalline metals by molecular dynamics simulation, *Nat. Mater.*, 2004, **3**, 43–47.
- 12 K. J. Briston, A. G. Cullis and B. J. Inkson, Fabrication of a novel SEM microgripper by electrochemical and FIB techniques, *J. Micromech. Microeng.*, 2010, article number: 015028.
- 13 X. D. Li, H. S. Hao, C. J. Murphy and K. K. Caswell, Nanoindentation of silver nanowires, *Nano Lett.*, 2003, **3**, 1495–1498.
- 14 Y. Peng, T. Cullis and B. Inkson, Bottom-up nanoconstruction by the welding of individual metallic nanoobjects using nanoscale solder, *Nano Lett.*, 2009, **9**, 91–96.
- 15 Z. Saghi, X. J. Xu and G. Mobus, Model based atomic resolution tomography, *J. Appl. Phys.*, 2009, **106**, article number: 024304.
- 16 G. Mobus and B. J. Inkson, Nanoscale tomography in materials science, *Mater. Today*, 2007, **10**, 18–25.
- 17 R. Agrawal, B. Peng and H. D. Espinosa, Experimental-computational investigation of ZnO nanowires strength and fracture, *Nano Lett.*, 2009, **9**, 4177–4183.
- 18 A. M. Walker, B. Slater, J. D. Gale and K. Wright, Predicting the structure of screw dislocations in nanoporous materials, *Nat. Mater.*, 2004, **3**, 715–720.
- 19 D. C. Sayle, X. D. Feng, Y. Ding, Z. L. Wang and T. X. T. Sayle, Simulating synthesis: ceria nanosphere self-assembly into nanorods and framework architectures, *J. Am. Chem. Soc.*, 2007, **129**, 7924–7935.
- 20 M. A. van Huis, L. T. Kunneman, K. Overgaag, Q. Xu, G. Pandraud, H. W. Zandbergen and D. Vanmaekelbergh, Low-temperature nanocrystal unification through rotations and relaxations probed by *in situ* transmission electron microscopy, *Nano Lett.*, 2008, **8**, 3959–3963.
- 21 T. X. T. Sayle, S. C. Parker and C. R. A. Catlow, The role of oxygen vacancies on ceria surfaces in the oxidation of carbon monoxide, *Surf. Sci.*, 1994, **316**, 329–336.
- 22 J. D. Gale, Gulp: capabilities and prospects, *Z. Kristallogr.*, 2005, **220**, 552–554.
- 23 D. C. Sayle, S. A. Maicananu and G. W. Watson, Atomistic models for $\text{CeO}_2(111)$, (110) , and (100) nanoparticles, supported on yttrium-stabilized zirconia, *J. Am. Chem. Soc.*, 2002, **124**, 11429–11439.

- 24 G. V. Lewis and C. R. A. Catlow, *J. Phys. C: Solid State Phys.*, 1985, **18**, 1149–1161.
- 25 T. X. T. Sayle and D. C. Sayle, Elastic deformation in ceria nanorods via a fluorite-to-rutile phase transition, *ACS Nano*, 2010, **4**, 879–886.
- 26 P. Martin, S. C. Parker, D. C. Sayle and G. W. Watson, Atomistic modeling of multilayered ceria nanotubes, *Nano Lett.*, 2007, **7**, 543–546.
- 27 G. Balducci, M. S. Islam, J. Kaspar, P. Fornasiero and M. Graziani, Bulk reduction and oxygen migration in the ceria-based oxides, *Chem. Mater.*, 2000, **12**, 677–681.
- 28 W. Smith and T. R. Forester, *DL_POLY*, Copyright by the Council for the Central Laboratory of the Research Councils, Daresbury Laboratory, Daresbury, Warrington, UK, 1996, www.cse.clrc.ac.uk/msi/software/DL_POLY/.
- 29 W. Humphrey, A. Dalke and K. Schulten, VMD—visual molecular dynamics, *J. Mol. Graphics*, 1996, **14**, 33–38.
- 30 N. Du, H. Zhang, B. G. Chen, X. Y. Ma and D. R. Yang, Ligand-free self-assembly of ceria nanocrystals into nanorods by oriented attachment at low temperature, *J. Phys. Chem. C*, 2007, **111**, 12677–12680.
- 31 Q. Zhang, S. J. Liu and S. H. Yu, Recent advances in oriented attachment growth and synthesis of functional materials: concept, evidence, mechanism, and future, *J. Mater. Chem.*, 2009, **19**, 191–207.
- 32 W. G. Hoover, *Phys. Rev. A: At., Mol., Opt. Phys.*, 1985, **31**, 1695–1697.
- 33 G. Kresse and J. Hafner, *Ab initio* molecular-dynamics simulation of the liquid–metal–amorphous semiconductor transition in germanium, *Phys. Rev. B: Condens. Matter Mater. Phys.*, 1994, **49**, 14251–14269.
- 34 G. Kresse and J. Furthmüller, Efficiency of *ab initio* total energy calculations for metals and semiconductors using a plane-wave basis set, *Comput. Mater. Sci.*, 1996, **6**, 15–50.
- 35 P. E. Blöchl, Projector augmented-wave method, *Phys. Rev. B: Condens. Matter Mater. Phys.*, 1994, **50**, 17953–17979.
- 36 G. Kresse and D. Joubert, From ultrasoft pseudopotentials to the projector augmented-wave method, *Phys. Rev. B: Condens. Matter Mater. Phys.*, 1999, **59**, 1758–1775.
- 37 J. P. Perdew, K. Burke and M. Ernzerhof, Generalized gradient approximation made simple, *Phys. Rev. Lett.*, 1996, **77**, 3865–3868.
- 38 S. L. Dudarev, G. A. Botton, S. Y. Savrasov, C. J. Humphreys and A. P. Sutton, Electron-energy-loss spectra and the structural stability of nickel oxide: an LSDA+U study, *Phys. Rev. B: Condens. Matter Mater. Phys.*, 1998, **57**, 1505–1509.
- 39 V. I. Anisimov, J. Zaanen and O. K. Andersen, Band theory and Mott insulators: Hubbard U instead of Stoner I, *Phys. Rev. B: Condens. Matter Mater. Phys.*, 1991, **44**, 943–954.
- 40 M. Nolan, S. C. Parker and G. W. Watson, The electronic structure of oxygen vacancy defects at the low index surfaces of ceria, *Surf. Sci.*, 2005, **595**, 223–232; D. O. Scanlon, *J. Phys. Chem. C*, 2009, **113**, 11095–11103.
- 41 A. Vantomme, Z. Y. Yuan, G. H. Du and B. L. Su, Surfactant-assisted large-scale preparation of crystalline CeO₂ nanorods, *Langmuir*, 2005, **21**, 1132–1135.
- 42 J. C. Conesa, Computer modelling of surfaces and defects on cerium dioxide, *Surf. Sci.*, 1995, **339**, 337–352.
- 43 A. S. Karakoti, S. V. N. T. Kuchibhatla, D. R. Baer, S. Thevuthasan, D. C. Sayle and S. Seal, Self-assembly of cerium oxide nanostructures in ice molds, *Small*, 2008, **4**, 1210–1216.
- 44 G. W. Watson, E. T. Kelsey, N. H. de Leeuw, D. J. Harris and S. C. Parker, *J. Chem. Soc., Faraday Trans.*, 1996, **92**, 433–438.
- 45 A. J. Lockwood and B. J. Inkson, *In situ* TEM nanoindentation and deformation of Si-nanoparticle clusters, *J. Phys. D: Appl. Phys.*, 2009, **42**, article number: 035410.
- 46 J. Wang, A. J. Kulkarni, F. J. Ke, Y. L. Bai and M. Zhou, Novel mechanical behavior of ZnO nanorods, *Comput. Meth. Appl. Mech. Eng.*, 2008, **197**, 3182–3189.
- 47 Z. W. Wang, S. Seal, S. Patil, C. S. Zha and Q. Xue, Anomalous quasihydrostaticity and enhanced structural stability of 3 nm nanoceria, *J. Phys. Chem. C*, 2007, **111**, 11756–11759.
- 48 X. D. Han, Y. F. Zhang, K. Zheng, X. N. Zhang, Z. Zhang, Y. J. Hao, X. Y. Guo, J. Yuan and Z. L. Wang, Low-temperature *in situ* large strain plasticity of ceramic SiC nanowires and its atomic-scale mechanism, *Nano Lett.*, 2007, **7**, 452–457.
- 49 J. Wang, A. J. Kulkarni, K. Sarasamak, S. Limpijumnong, F. J. Ke and M. Zhou, Molecular dynamics and density functional studies of a body-centered-tetragonal polymorph of ZnO, *Phys. Rev. B: Condens. Matter Mater. Phys.*, 2007, **76**, 172103.
- 50 J. A. Kulkarni, M. Zhou, K. Sarasamak and S. Limpijumnong, Novel phase transformation in ZnO nanowires under tensile loading, *Phys. Rev. Lett.*, 2006, **97**, 105502.
- 51 W. Sangthong, J. Limtrakul, F. Illas and S. T. Bromley, Persistence of magic cluster stability in ultra-thin semiconductor nanorods, *Nanoscale*, 2010, **2**, 72–77.